Soft Matter



PAPER



Cite this: Soft Matter, 2020, **16**, 3005

Received 7th January 2020, Accepted 14th February 2020

DOI: 10.1039/d0sm00043d

rsc.li/soft-matter-journal

Nanorod position and orientation in vertical cylinder block copolymer films†

Boris Rasin, 📭 Benjamin J. Lindsay, Singchen Ye, Jeffrey S. Meth, Christopher B. Murray, ac Robert A. Riggleman b and Russell J. Composto b *a

The self-assembly of gold nanorods (AuNRs) of different sizes with a block copolymer (BCP) is studied. Polystyrene-block-poly(2-vinylpyridine) (PS-b-P2VP) films containing P2VP functionalized AuNRs are solvent annealed resulting in a BCP morphology of vertical P2VP cylinders in a PS matrix. At the surface of the PS-b-P2VP films long AuNRs are found in the bridging and vertical states. The bridging state is where the long axis of the AuNR is parallel to the film surface, the AuNR is embedded in the film, and each end of the AuNR is at the top of nearest neighbor P2VP cylinders. The vertical state is where the AuNR is localized within a vertical P2VP cylinder, the AuNR long axis is perpendicular to the film surface and the upper tip of the AuNR is at the film surface. Short AuNRs were found in the bridging and vertical states as well as in a state not observed for the long AuNRs, the centered state. The centered state is where an AuNR has its long axis parallel to the film surface, is embedded in the film, and is centered over a vertical P2VP cylinder. Hybrid particle-field theory (HPFT) simulations modeling the experimental system predict that for the long AuNRs only the bridging state should be observed while for the short AuNRs only the bridging and centered states should be observed. Possible explanations for why the vertical state is observed in experiments despite being thermodynamically unfavorable in simulations are discussed. HPFT simulations also show that when a nanorod is in the bridging state the two cylinders it bridges remain intact and extend from the nanorod to the substrate. Further, the minority block of the BCP is shown to wet the bottom of the bridging nanorod. The bridging state is very promising for the future development of self-assembled nanoscale devices.

Introduction

Nanoparticle-block copolymer (NP-BCP) self-assembly is a powerful approach for controlling NP position and orientation in polymer nanocomposites (PNCs). Control of NP position and orientation in PNCs allows the fabrication of PNC devices and the engineering of PNC properties. For example, metal NPs could be positioned in PNCs to form chains of non-touching metal NPs, resulting in metal NP plasmon waveguides. Thus, it

is important to continue to improve our understanding of and to continue to develop NP-BCP self-assembly.

NP-BCP self-assembly is typically implemented by solvent annealing or thermal annealing a PNC consisting of NPs and a BCP. The BCP self-assembles into a periodic morphology; for example a linear diblock copolymer can self-assemble into a hexagonal lattice of cylinders formed from one block in a matrix of the other block.² The NPs assume specific positions and orientations in the BCP morphology.3 For example, NPs can be localized in the microdomains formed by one of the blocks or be located at the interfaces between microdomains.⁴

Spherical NP-BCP self-assembly has been extensively studied. 4-11 By comparison, studies of nanorod-BCP self-assembly are an emerging area of research. 12-22 In this work we study the position and orientation of nanorods in vertical cylinder BCP films. Nanocomposite films of polystyrene-block-poly(2-vinylpyridine) (PS-b-P2VP) and P2VP functionalized gold nanorods (AuNRs) were solvent annealed resulting in the PS-b-P2VP assuming a morphology of vertical P2VP cylinders in a PS matrix. At the surface of films prepared with long AuNRs, AuNRs were in the bridging and vertical states. The bridging state is where the long axis of the AuNR is parallel to the film surface, the AuNR is embedded in the film, and each end of the AuNR is at the top of

^a Department of Materials Science and Engineering, University of Pennsylvania, Philadelphia, Pennsylvania 19104, USA. E-mail: composto@seas.upenn.edu

^b Department of Chemical and Biomolecular Engineering, University of Pennsylvania, Philadelphia, Pennsylvania 19104, USA

^c Department of Chemistry, University of Pennsylvania, Philadelphia, Pennsylvania 19104, USA

^d DuPont Co., Wilmington, Delaware 19803, USA

[†] Electronic supplementary information (ESI) available: AFM images of neat as-spincoated PS-b-P2VP films; AFM images of neat PS-b-P2VP films solvent annealed for various lengths of time; TEM image of the 101 nm length by 16 nm diameter AuNRs; UV-vis-NIR spectrum of the 101 nm length by 16 nm diameter AuNRs; diagram for identifying that a bridging AuNR is not at a defect in the hexagonal lattice; diagram for identifying that a centered AuNR is not at a defect in the hexagonal lattice; HPFT simulation results for $1.5R_{\rm g}$ and $2R_{\rm g}$ diameter nanorods; additional model details (PDF). See DOI: 10.1039/d0sm00043d

Soft Matter **Paper**

nearest neighbor vertical cylinders. The vertical state is where the long axis of the AuNR is perpendicular to the film surface, the AuNR is localized in a vertical cylinder, and the upper tip of the AuNR is at the film surface. At the surface of films prepared with shorter AuNRs, AuNRs were found in the bridging, vertical, and centered states. The centered state is where the long axis of the AuNR is parallel to the film surface, the AuNR is embedded in the film and the AuNR is located on top of one vertical P2VP cylinder. As the nanorods assume specific states at the surface of the BCP films and the states assumed are shown to depend on the nanorod dimensions, control over nanorod position and orientation is demonstrated.

The free energy of the bridging, centered and vertical states as a function of nanorod length was calculated with hybrid particle-field theory (HPFT) simulations. At the surface of films containing the long AuNRs, the simulations predicted that only the bridging state should be observed, whereas both the bridging and centered states were predicted for shorter AuNRs. The simulations also predicted that the vertical state should not be observed. HPFT simulations were also used to study the BCP morphology when a nanorod is in the bridging state. The simulations showed that when an AuNR is in the bridging state, the bridged vertical cylinders remain intact and there is a minority block wetting layer underneath the AuNR.

Results and discussion

Neat PS-b-P2VP films with a vertical cylinder morphology

Neat PS-b-P2VP films with a morphology of vertical P2VP cylinders in a PS matrix were prepared via solvent annealing. The films were

prepared following the method of Yin et al. 23 A diblock copolymer of $PS(M_n = 180\,000 \text{ g mol}^{-1})-b-P2VP(M_n = 77\,000 \text{ g mol}^{-1})$ was spin-coated from chloroform on silicon wafers. The PS-b-P2VP films had a thickness of 363 nm. Atomic force microscopy (AFM) topography images of the as-spin-coated PS-b-P2VP films show a mixture of trenches and circular pits (Fig. S1, ESI†). To obtain a vertical cylinder morphology the films were solvent annealed in chloroform. During solvent annealing the PS-b-P2VP film absorbs chloroform and swells. The chloroform in the film reduces the BCP glass transition temperature which increases the mobility of the BCP chains and allows the film structure to change. 24-26

To determine the optimum solvent annealing time that produces a vertical cylinder morphology, films were solvent annealed from 7:30 (min:s) to 17:30. AFM topography images of the surfaces after solvent annealing show that films annealed between 13:45 and 16:15 have a surface topography of circular depressions forming a hexagonal lattice (Fig. S2, ESI†).

Films solvent annealed for 14:23 were further analyzed and later selected for the polymer nanocomposite studies. AFM topography images of PS-b-P2VP films solvent annealed for 14:23 show a hexagonal lattice of circular depressions as seen in Fig. 1a. Fig. 1b shows a line profile passing through the centers of the depressions in a row of nearest neighbor depressions. The minima in the line profile correspond to the bottoms of the depressions. The average depth of the depressions was 11.5 nm.

To complement AFM studies, scanning electron microscopy (SEM) was used to characterize films solvent annealed for 14:23. Films were exposed to iodine vapor which selectively stains P2VP domains which appear brighter than PS domains

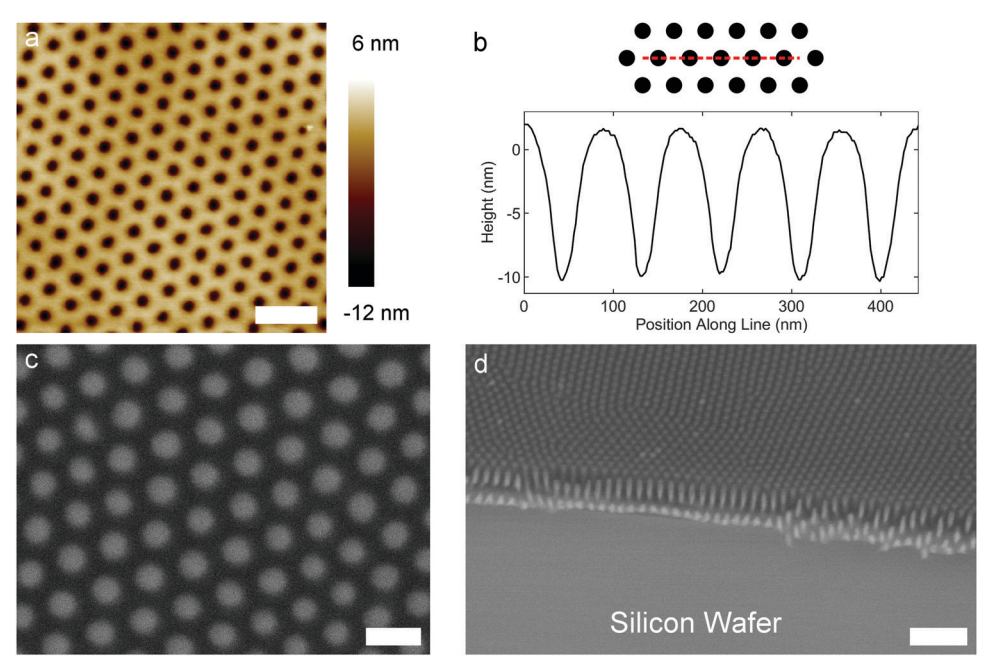


Fig. 1 Characterization of neat vertical cylinder PS-b-P2VP films prepared by solvent annealing for 14:23 (min:s). (a) AFM topography image. The lower (dark) circular regions are the tops of P2VP cylinders. The scale bar is 200 nm. (b) Line profile from the AFM image in (a) with the path of the line profile (dashed red line) relative to the tops of the P2VP cylinders shown in a schematic. (c) Top-down SEM image. The film was stained with iodine vapor causing the P2VP domains to appear brighter in the SEM image. The scale bar is 100 nm. (d) SEM image of a film cross-section. This film was also stained with iodine vapor prior to imaging. The scale bar is 500 nm.

Soft Matter **Paper**

in SEM. Fig. 1c, a top-down SEM image of a PS-b-P2VP film, shows circular features (light) forming a hexagonal lattice surrounded by a continuous region (dark). The silicon substrates supporting the films were cleaved to expose the film cross-section. Fig. 1d shows an SEM image of a film crosssection. Light stripes perpendicular to the film surface extend from the surface nearly to the bottom of the film. These stripes are regularly spaced and separated by darker regions. The white lines do not extend all the way to the substrate because the interface generated from the cleaving process is not the ideal flat vertical interface. The surface of the film, visible in the top half of Fig. 1d, is consistent with top-down SEM (Fig. 1c) with brighter circles forming a hexagonal lattice surrounded by a dark background.

From the top-down and cross-section SEM images we conclude that the morphology of the PS-b-P2VP films solvent annealed for 14:23 is vertical P2VP cylinders in a PS matrix with the vertical P2VP cylinders extending from the substrate to the film surface. In the top-down view the light circular features forming a hexagonal lattice are P2VP cylinders being viewed along their axis which is perpendicular to the film surface and the dark surrounding background is the PS matrix. The light stripes in the SEM cross-section are the vertical P2VP cylinders being viewed from the side. From the top-down SEM images we determined the P2VP cylinder diameter to be 43 nm. The center-to-center spacing between a cylinder and a nearest neighbor cylinder was 83 nm. With the morphology of the film elucidated from SEM, it is clear that the hexagonally arranged depressions observed in AFM topography images are the tops of vertical P2VP cylinders and the higher surrounding region is the PS matrix. Our hypothesis for why the tops of the P2VP cylinders are 11.5 nm deep depressions is as follows. Elbs and Krausch showed that when exposed to chloroform vapor P2VP films increase in thickness more than PS films.²⁷ Consequently, when

our PS-b-P2VP films are solvent annealed in chloroform the volume fraction of chloroform in the P2VP domains is greater than the volume fraction of chloroform in the PS domains. As a result when the chloroform evaporates the volume of the P2VP domains decreases more than the volume of the PS domains resulting in the formation of basins at the top of the P2VP cylinders. All nanocomposite films described in this study were solvent annealed for 14:23.

Position and orientation of AuNRs in PS-b-P2VP films with a vertical cylinder morphology

The position and orientation of AuNRs functionalized with P2VP in vertical cylinder PS-b-P2VP films was studied. Nanocomposite films consisting of PS-b-P2VP and AuNRs were prepared by spin-coating a solution of PS-b-P2VP and AuNRs grafted with thiol-terminated $P2VP(M_n = 2500 \text{ g mol}^{-1})$ in chloroform on silicon wafers. Nanocomposite films were prepared with AuNRs of two different sizes. One set of nanocomposites was prepared with AuNRs with a length of 101 nm and a diameter of 16 nm. The other set of nanocomposites was prepared with AuNRs with a length of 70 nm and a diameter of 12 nm. Both sets of nanocomposites had an AuNR weight fraction of 0.01 which corresponds to an AuNR volume fraction of 5.6 \times 10⁻⁴. After spin-coating, the nanocomposite films were solvent annealed in chloroform for 14:23. We will denote the solvent annealed PS-b-P2VP-(101 nm length by 16 nm diameter AuNR) nanocomposites as PS-b-P2VP-AuNR101 and the solvent annealed PS-b-P2VP-(70 nm length by 12 nm diameter AuNR) nanocomposites as PS-b-P2VP-AuNR70.

Position and orientation of AuNRs in PS-b-P2VP-AuNR101 films

AFM characterization was performed on PS-b-P2VP-AuNR101 films. As shown in Fig. 2a, the topography images of the surface show a similar structure as the neat films (Fig. 1a), namely a

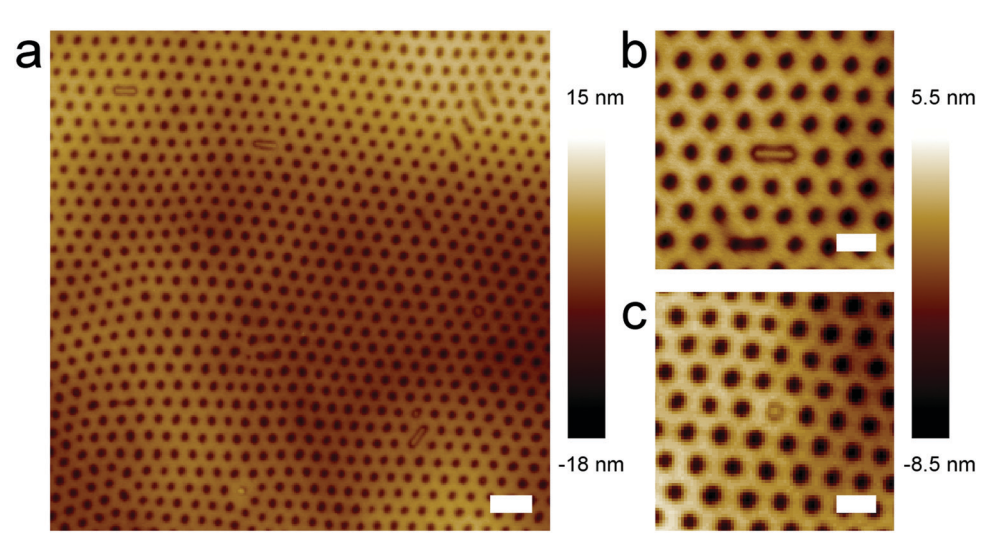


Fig. 2 AFM topography images of the surface of PS-b-P2VP-AuNR101 films. (a) Large area AFM image showing three AuNRs in the bridging state. A circular feature can also be observed at the top of some vertical cylinders. The scale bar is 200 nm. (b) AFM image of an AuNR in the bridging state not at a defect in the vertical cylinder lattice. The AuNR is the same AuNR as that in the top left corner of image (a). The scale bar is 100 nm. (c) AFM image of a circular feature colocalized with a vertical P2VP cylinder. The scale bar is 100 nm.

hexagonal lattice of circular depressions. This result suggests that PS-b-P2VP-AuNR101 films have a morphology of vertical P2VP cylinders in a PS matrix with the depressions at the surface corresponding to the tops of vertical P2VP cylinders and the surrounding higher region corresponding to the PS matrix. We found that the circular depressions on the surface had a depth of 7.8 nm which is shallower than the value for the neat films, 11.5 nm. AuNRs are observed at the surface of PS-b-P2VP-AuNR101 films in the AFM topography images (Fig. 2a and b). We found that 95% of AuNRs at the surface were in the "bridging state" shown in Fig. 2b. The bridging state is where the AuNR is embedded in the film, the AuNR long axis is parallel to the film surface and one end of the AuNR is at the top of a given P2VP cylinder while the other end is at the top of a P2VP cylinder that is a nearest neighbor of the given P2VP cylinder. We found that 63% of AuNRs in the bridging state were not at a defect in the hexagonal lattice. Our definition for an AuNR not at a defect in the hexagonal lattice is given in the Methods. Fig. 2b shows an AFM image of an AuNR in the bridging state not at a defect in the hexagonal lattice, whereas Fig. 3 shows an AFM image of an AuNR in the bridging state at a defect in the hexagonal lattice. The 5% of AuNRs at the surface not in the bridging state were embedded in the film and their long axis was parallel to the film surface. However, the lattice around these AuNRs was so defective that we could not determine whether the AuNRs were bridging vertical cylinders or in a different state.

The position and orientation of bridging AuNRs that are not at a defect in the hexagonal lattice is analyzed in greater detail. From AFM images (*e.g.*, Fig. 2b), the top of the AuNRs, defined as the midpoint of the line defined by the crest of the AuNR, was on average 1.6 nm below the PS matrix. Fig. 4 is a line profile along the crest of a bridging AuNR not at a defect in the lattice which shows the relative heights of the top of the AuNR (center of image) and the PS matrix (continuous phase). Further we observed that the region immediately surrounding the AuNRs was 2.0 nm lower than the top of the AuNRs. The AuNRs were almost completely parallel to the surface with an average

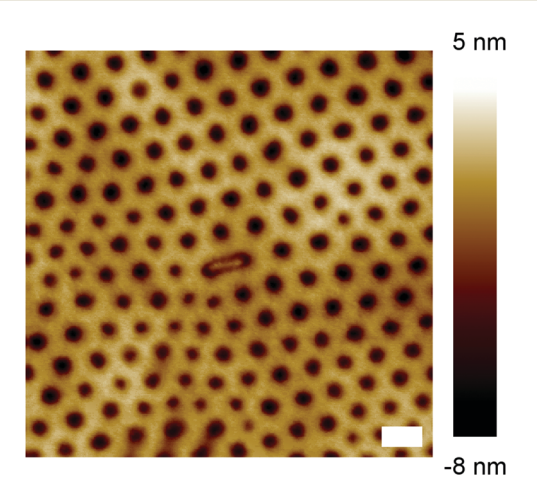


Fig. 3 AFM topography image of an AuNR in the bridging state at a defect in the vertical cylinder lattice. The scale bar is 100 nm.

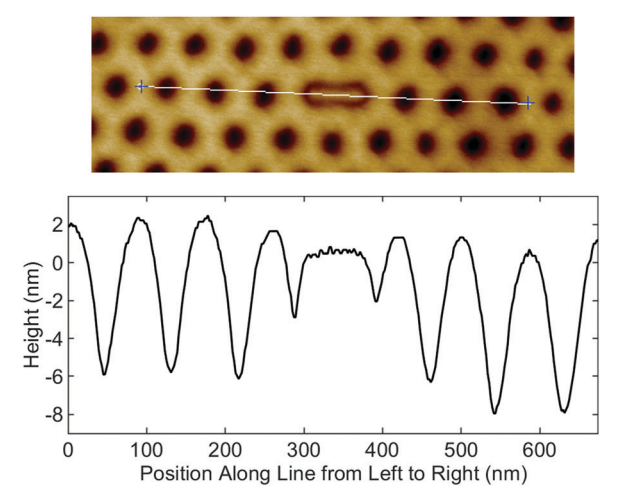


Fig. 4 Line profile from the AFM image in Fig. 2b along the crest of the AuNR in the bridging state not at a defect in the vertical cylinder lattice. The path of the line profile is shown *via* a line on the AFM image at the top of the figure.

angle between the long axis of the AuNR and the surface of 0.9°. This can be seen in the line profile in Fig. 4. Like the bridging AuNRs not at a defect in the hexagonal lattice the bridging AuNRs at defects in the hexagonal lattice were almost completely parallel to the surface. However, the top of these AuNRs varied from 1 nm above the PS matrix to below the PS matrix.

The AFM topography images of the surface of the PS-*b*-P2VP-AuNR101 films also show that some vertical cylinders have a circular feature at their top as shown in Fig. 2c. One explanation is that the circular feature corresponds to a vertically oriented AuNR localized within a P2VP cylinder and positioned with its upper tip at the film surface. A second explanation is that a circular feature is a gold nanosphere localized within a P2VP cylinder and positioned at the film surface. Gold nanospheres are present in the PS-*b*-P2VP-AuNR101 films as they are a very minor product in AuNR synthesis.

Top-down SEM images of the PS-b-P2VP-AuNR101 films show that there are AuNRs at the surface of the films and that the AuNRs are parallel to the surface of the films (Fig. 5). These observations are consistent with AFM studies shown in Fig. 2. Nanoparticles below the surface of a film appear blurry while those at the surface of a film are sharp allowing us to determine whether a nanoparticle is at or below the surface of a film. Circular features are also observed at the surface of the films matching our observation of circular features colocalized with vertical P2VP cylinders in AFM images. The SEM images show AuNRs that are not vertically oriented below the surface of the films. This shows that there are AuNRs below the surface of the films that are not localized within vertically oriented P2VP cylinders. Circular features are also observed below the surface of the films. These features could be vertically oriented AuNRs or gold nanospheres.

We also examined the cross-sections of the PS-*b*-P2VP-AuNR101 films with SEM (Fig. 6). The SEM images show that at the surface of the films there are vertical AuNRs with their tip

Soft Matter **Paper**

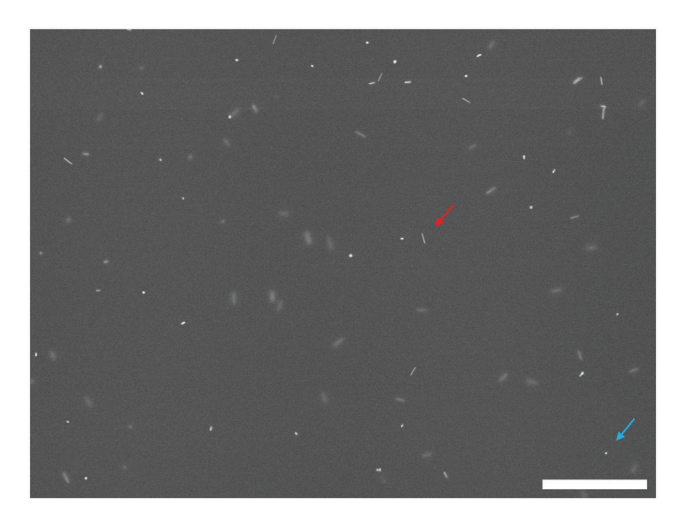


Fig. 5 Top-down SEM image of a PS-b-P2VP-AuNR101 film. The red arrow points to a nanorod at the film surface that is parallel to the film surface. The blue arrow points to a circular feature at the film surface. The scale bar is 1 um.



Fig. 6 SEM image of the cross-section of a PS-b-P2VP-AuNR101 film. The blue arrows point to vertically oriented AuNRs with their tip at the surface of the film. The scale bar is $1 \mu m$.

at the surface of the film (blue arrows in Fig. 6). The SEM images also show AuNRs parallel to the surface of the films at the surface of the films and circular features at the surface of the films. Our observation of a circular feature at the top of some vertical cylinders in AFM suggests that the vertical AuNRs at the surface of the film are localized within a vertical P2VP cylinder. The observation of AuNRs parallel to the film surface at the film surface matches our AFM and top-down SEM results. Circular features observed at the film surface could be either gold nanospheres or AuNRs being viewed end-on. AuNRs are also observed in the films. AuNRs in the films have many different orientations showing that AuNRs in the films are not localized within vertical P2VP cylinders. Circular features are observed in the films which could be either gold nanospheres or AuNRs being viewed end-on.

Position and orientation of AuNRs in PS-b-P2VP-AuNR70 films

The surfaces of PS-b-P2VP-AuNR70 nanocomposite films were characterized with AFM. As shown in Fig. 7a, AFM topography images of the film surface show the same hexagonal lattice of circular depressions observed in the AFM topography images of the neat films (Fig. 1a). This result suggests that the nanocomposite films have a morphology of vertical P2VP cylinders in a PS matrix. The depressions are the tops of vertical P2VP cylinders and the surrounding region is the PS matrix. The depth of the circular depressions at the surface of the PS-b-P2VP-AuNR70 nanocomposite films was 9.6 nm which was less

than the depth of the circular depressions at the surface of neat vertical cylinder films.

As seen in Fig. 7a, AFM topography images show AuNRs at the surface of the PS-b-P2VP-AuNR70 films. AuNRs in the bridging state are observed as shown in Fig. 7a-c. AuNRs are also observed in the "centered state", which can be seen in Fig. 7a and d. The centered state is where an AuNR is positioned over a single P2VP cylinder, embedded in the film, and the long axis of the AuNR is parallel to the surface of the film. We found that 75% of AuNRs were in the bridging state and that 22% of AuNRs were in the centered state. Of the bridging AuNRs, 80% were not at a defect in the lattice and 77% of the centered AuNRs were not at a defect in the lattice. The definitions for bridging and centered AuNRs not at a defect in the lattice are given in the Methods. The 3% of AuNRs not in the centered or bridging states are embedded in the film surface and parallel to the film surface, however, the lattice around the AuNRs had so many defects that it could not be determined whether they were in a bridging, centered, or other state.

We analyzed AuNRs in the bridging state not at a defect in the lattice. The top of these AuNRs, measuring from the midpoint of the line defined by the crest of the AuNR, was on average 1.7 nm below the PS matrix. The average angle of the AuNRs long axis relative to the surface of the film was 2.3°, showing that the AuNRs were parallel to the film surface. Further, we found the region around the AuNRs to be on average 1.5 nm below the top of the AuNRs. Like the AuNRs in the bridging state not at a defect in the lattice, the AuNRs in the bridging state at a defect in the lattice were parallel to the film surface and had their tops below the film surface.

AuNRs in the centered state not at a defect in the lattice were analyzed. The AuNRs top, measuring from the midpoint of the line defined by the crest of the AuNR, was on average 0.6 nm below the PS matrix. The top of the AuNRs was essentially level with the PS matrix. The AuNRs were parallel to the film surface with an average angle of 1.8° between the long axis of the AuNRs and the surface of the film. AuNRs in the centered state at a defect in the lattice also had their tops level with the PS matrix and their long axis was parallel to the film surface.

The AFM images of the PS-b-P2VP-AuNR70 films also show that some vertical P2VP cylinders have a circular feature located at their top (Fig. 7e). This was also observed for the PS-b-P2VP-AuNR101 films. As for the PS-b-P2VP-AuNR101 films, possible explanations for the circular features are that they are the end of a vertically oriented AuNR localized within a vertical P2VP cylinder or that they are a spherical nanoparticle localized within a vertical P2VP cylinder.

The PS-b-P2VP-AuNR70 films were further characterized with SEM. Top-down SEM images show that there are AuNRs at the surface of the films and these AuNRs are parallel to the surface of the film (Fig. 8). Top-down SEM images also show circular features at the surface. The presence of parallel AuNRs and circular features at the surface matches our AFM results. Top-down SEM images also show that there are nanorods below the film surface that are not vertically oriented and that there are circular features below the film surface. The presence of

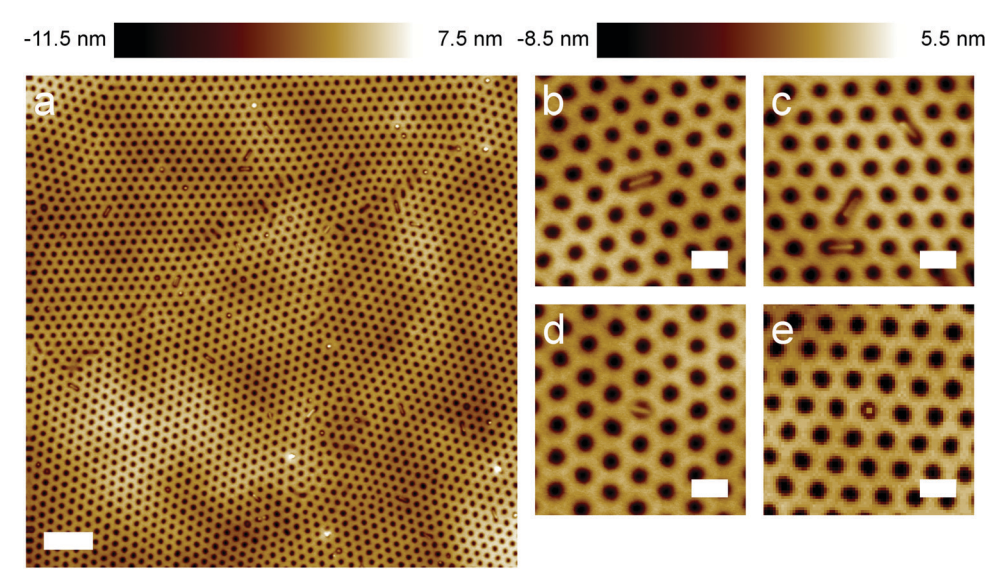


Fig. 7 AFM topography images of the surface of PS-b-P2VP-AuNR70 films. (a) Large area AFM image showing AuNRs in the bridging and centered states. The image also shows a circular feature at the top of some vertical cylinders. The scale bar is 400 nm. (b) AFM image of an AuNR in the bridging state not at a defect in the vertical cylinder lattice. The scale bar is 100 nm. (c) AFM image of multiple AuNRs in the bridging state. The same AuNRs can be observed at the top middle of (a). The scale bar is 100 nm. (d) AFM image of an AuNR in the centered state not at a defect in the vertical cylinder lattice. The scale bar is 100 nm. (e) AFM image of a circular feature colocalized with a vertical P2VP cylinder. The scale bar is 100 nm.

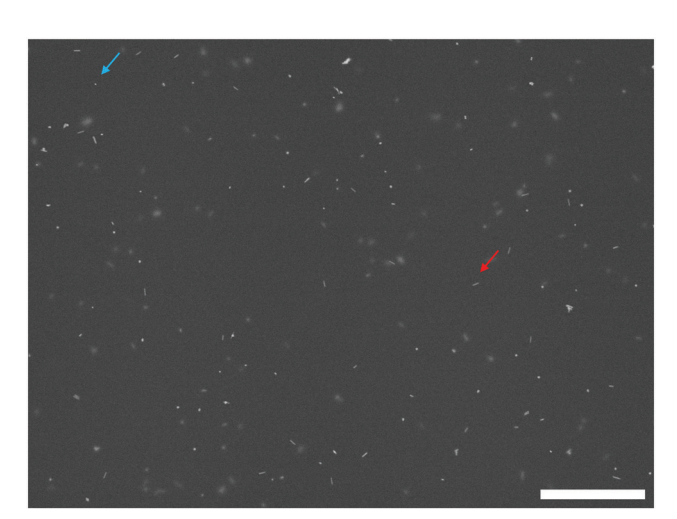


Fig. 8 Top-down SEM image of a PS-b-P2VP-AuNR70 film. The red arrow points to a nanorod at the film surface that is parallel to the film surface. The blue arrow points to a circular feature at the film surface. The scale bar is 1 μ m.

nanorods below the film surface that are not vertically oriented indicates that there are nanorods below the film surface that are not localized within vertical P2VP cylinders. The circular features below the film surface could either be gold nanospheres or vertically oriented AuNRs.

SEM images of the film cross-sections show vertically oriented AuNRs in the films with their top end at the film surface (blue arrow in Fig. 9). In our AFM images we observed that some vertical cylinders had a circular feature at their top. Thus, we can conclude that the vertical AuNRs with their top end at the film surface are localized in vertical P2VP cylinders.



Fig. 9 SEM image of the cross-section of a PS-b-P2VP-AuNR70 film. The blue arrow points to a vertically oriented AuNR with its tip at the surface of the film. The scale bar is 1 μ m.

AuNRs parallel to the film surface are also observed at the film surface in cross-sectional SEM images in agreement with our AFM results. In addition, circular features are observed at the film surface. These features could be attributed to an AuNR viewed end-on or a gold nanosphere. The cross-section SEM images show that inside the films AuNRs have many different orientations suggesting that these AuNRs are not localized in vertical P2VP cylinders. Also observed inside the films are circular features which could be attributed to AuNRs being viewed end-on or gold nanospheres.

Hybrid particle-field theory simulations

AFM and SEM results showed that AuNRs at the surface of PS-*b*-P2VP-AuNR101 films are either bridging or vertical while AuNRs at the surface of PS-*b*-P2VP-AuNR70 films are either bridging, centered or vertical. To understand how AuNRs distribute between the bridging, centered and vertical states in the PS-*b*-P2VP-AuNR101 and PS-*b*-P2VP-AuNR70 films, HPFT simulations were performed. In the simulations a single nanorod was placed into a vertical cylinder diblock copolymer film representative of experimental films in either the bridging state, the centered state, or the vertical state and the free energy of the system was calculated. For each state, the free energy of

Soft Matter Paper

the system was calculated as a function of nanorod length relative to the center-to-center distance between P2VP domains.

For the simulated neat diblock copolymer film, the vertical cylinders had a nearest-neighbor center-to-center distance $r_{\rm ctc}$ of $5.09R_g$ and a diameter of $2.85R_g$, where R_g is the ideal radius of gyration of the diblock copolymer. The thickness of the HPFT simulation film was $9R_g$, which is sufficiently thick for the interfaces to not interact. For comparison in our experimental system the center-to-center distance between nearest-neighbor vertical cylinders was $6.03R_{\rm g,exp}$, the cylinder diameter was $3.12R_{\rm g,exp}$, and the film thickness was $26.36R_{\rm g,exp}$ where $R_{\rm g,exp}$ 77 000 g mol⁻¹). Assuming Gaussian chain statistics with equal statistical segments sizes for both blocks, we calculate $R_{g,exp}$ = 13.8 nm using $b_{\text{exp}} = 0.68 \text{ nm.}^{28}$ The difference in parameters in the calculations and the experiments is due to the difference in χ values expected in the experiments and employed in the simulations, which leads to a larger domain spacing relative to the neat polymer $R_{\rm g}$.

Since in the experiments the AuNRs are densely functionalized with short P2VP ligands, in our HPFT simulations we model the nanorod as though it has the same chemistry as the minority block of the copolymer, resulting in an athermal nanorod–monomer interaction with the cylinder-forming block. The simulations were performed with a nanorod of $1R_{\rm g}$ diameter as this diameter is representative of the diameters of the AuNRs used in experiments (12 nm and 16 nm). In the experimental system in terms of $R_{\rm g,exp}$ the diameter of the 12 nm diameter AuNRs was $0.87R_{\rm g,exp}$ and the diameter of the 16 nm diameter AuNRs was $1.16R_{\rm g,exp}$. For the bridging, centered, and vertical states, Fig. 10 shows the system free energy, ΔF , as a function of nanorod length, $L_{\rm NR}$, normalized by $r_{\rm ctc}$. The free energy ΔF in $k_{\rm B}T$ is taken relative to the free

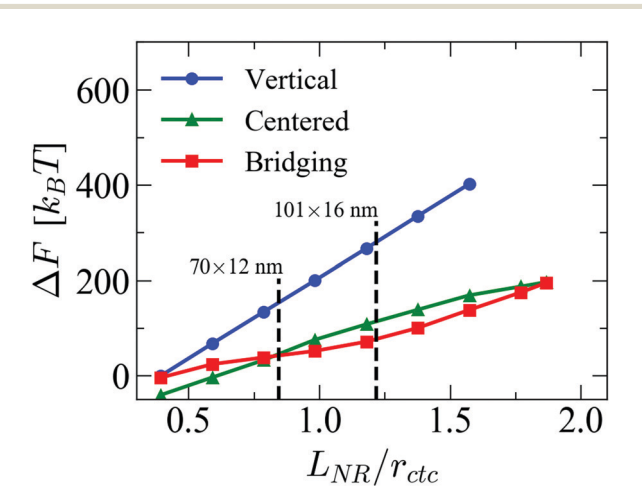


Fig. 10 Free energy for nanorods of diameter $1R_{\rm g}$ in the bridging, centered, and vertical states as a function of nanorod length. The nanorod length, $L_{\rm NR}$, is normalized by the vertical cylinder nearest-neighbor center-to-center distance, $r_{\rm ctc}$. The free energy is taken relative to the free energy of a nanorod of diameter $1R_{\rm g}$ and length $2R_{\rm g}$ in the vertical state. The free energies for PS-b-P2VP-AuNR70 and PS-b-P2VP-AuNR101 films are denoted by vertical dashed lines.

energy of a vertical nanorod with a diameter and length of $1R_g$ and $2R_g$, respectively.

The HPFT simulation predictions can be compared with the two experimental systems. For the PS-b-P2VP-AuNR101 experimental system L_{NR}/r_{ctc} = 1.22 (right vertical dashed line in Fig. 10). At this $L_{\rm NR}/r_{\rm ctc}$ Fig. 10 shows that the bridging state is thermodynamically favored, while the centered state is less favorable and the vertical state is even more unfavorable. Using the Boltzmann distribution and interpolated values of ΔF at $L_{\rm NR}/r_{\rm ctc}$ = 1.22 to estimate relative populations, HPFT simulations predict that virtually all AuNRs should be in the bridging state, with negligible centered and vertical fractions of 8.7 \times 10^{-17} and 2.9×10^{-89} . Comparing the HPFT simulations with the experimental horizontal states, only the bridging state is observed in PS-b-P2VP-AuNR101 films consistent with HPFT simulations. However, whereas HPFT simulations predict that the vertical state is unfavorable, experiments (i.e., AFM and SEM) show that there are AuNRs in the vertical state in PS-b-P2VP-AuNR101 films. This could be due to fluctuation effects that are neglected in the HPFT simulation calculations, or it could be a result of the solvent annealing processing used to generate the experimental systems.

For PS-b-P2VP-AuNR70 films $L_{\rm NR}/r_{\rm ctc}=0.84$ (left vertical dashed line in Fig. 10). At $L_{\rm NR}/r_{\rm ctc} = 0.84$ Fig. 10 shows that the bridging state is slightly more favored than the centered state and the vertical state is the least thermodynamically favored state. Using the Boltzmann distribution and ΔF at $L_{\rm NR}/r_{\rm ctc}$ = 0.84 to estimate relative populations, we expect a non-negligible fraction of centered nanorods, where the ratio of bridging to centered nanorods is about 12:1. The vertical state is again expected to be negligible with a vertical fraction of about 1.3 imes 10 $^{-48}$. In PS-b-P2VP-AuNR70 films, AuNRs are observed in the bridging, the centered and the vertical state with the ratio of the bridging to centered states being 3.5:1. It is important to note that this ratio is the ratio of bridging rods away from defects to centered rods away from defects as previously discussed. The simulation results trend in a similar direction with the experiments in that the centered state is more preferable for the shorter nanorods than for the longer ones. However, the results are not in quantitative agreement with the experiments.

In addition to the results with a nanorod diameter of $1R_{\rm g}$ (Fig. 10), HPFT simulations were used to calculate the free energy for thicker nanorods, with diameters of $1.5R_{\rm g}$ and $2R_{\rm g}$ as shown in Fig. S7b and c (ESI†), respectively. Briefly, we find that the range of $L_{\rm NR}/r_{\rm ctc}$ where bridging is favored grows with increasing diameter, and the range where centered is favored decreases

There are several possible explanations for the differences between experiments and HPFT simulation predictions. First, nanocomposite films were processed *via* solvent annealing where the BCP and the AuNRs co-assemble during swelling and solvent evaporation. As a result, AuNRs in the dry film may be kinetically trapped in thermodynamically unfavorable or metastable states.²⁹ Due to the mean-field nature of the calculations, these kinetic effects are not represented in

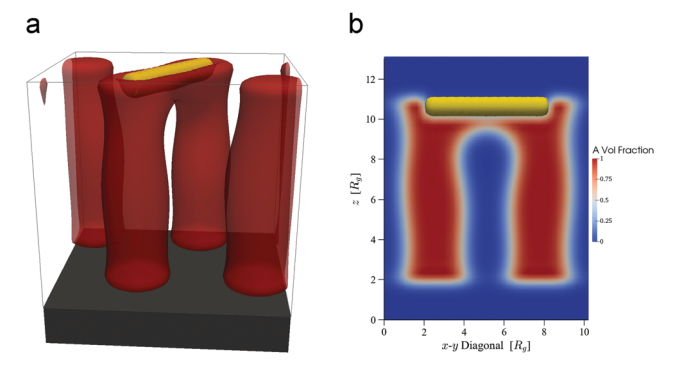


Fig. 11 For a nanorod of diameter $1R_{\rm g}$ and length $6R_{\rm g}$ in the bridging state (a) shows the isosurface (red) of 0.5 local volume fraction of block A and (b) shows the local A block volume fraction in a 2D slice along the length of the nanorod. The A block is the cylinder forming block.

the simulations. Second, the simulations do not explicitly model the grafted polymers, and therefore these calculations would not capture any entropy associated with the grafted polymers that may be important. Finally, the experimental χN parameter is larger than those used in the simulations and we have assumed equal interactions (surface energy) of both blocks with the top surface.

Simulations were also used to reveal the morphology of the BCP when a nanorod is in the bridging state. Fig. 11a and b show the 3D field configuration and a 2D slice along the length of the nanorod for a nanorod in the bridging state with diameter and length of $1R_g$ and $6R_g$. These nanorod dimensions approximately correspond to the 101 nm length by 16 nm diameter AuNRs in the PS-b-P2VP-AuNR101 films. Both representations show that minority blocks wet the underside of the bridging nanorod resulting in the two bridged vertical cylinders becoming connected into one arch shaped domain. The vertical cylinders forming each "column" of the arch remain intact. Characterization of the wetting layer is not experimentally accessible, emphasizing the importance of using HPFT simulations to interpret experimental results. In summary, HPFT simulations reveal that when an AuNR bridges two vertical cylinders that the domains remain intact below the surface and a wetting layer is formed beneath the nanorod.

Conclusions

The ability to control the position and orientation of nanorods at the surface of self-assembled vertical block copolymer cylindernanorod nanocomposites is demonstrated. The longer nanorods either bridge vertical cylinders at the surface or are localized within vertical cylinders with their tip at the film surface. In addition to the two states assumed by the longer nanorods, shorter nanorods assume a state where they are centered at the top of one vertical cylinder. HPFT simulations provided the relative free energies of the three states as a function of nanorod length and provided insight into the polymer morphology when a nanorod was in the bridging state. The bridging state observed in this work has many potential applications in self-assembled nanoscale devices.

Further, to our knowledge this work demonstrates the first example of controlling nanoparticle position and orientation in a BCP *via* the bridging of two domains separated by a third domain. This is a promising approach for developing new devices and materials with desired properties.

Methods

Synthesis of 101 nm length by 16 nm diameter AuNRs

The AuNRs were synthesized according to Ye *et al.* ³⁰ The AuNRs were imaged with transmission electron microscopy (TEM) (JEOL JSM-7500F Field Emission Scanning Electron Microscope, Transmission Electron Detector) and the nanorod dimensions were determined from the TEM images (Fig. S3, ESI†). The AuNRs were also characterized with UV-vis-NIR spectroscopy (Fig. S4, ESI†) (Varian Cary 5000 UV-Vis-NIR Spectrophotometer).

Preparation and characterization of neat vertical cylinder PS-b-P2VP films

Neat vertical cylinder PS-*b*-P2VP films were prepared following Yin *et al.*²³ A 2 wt% PS($M_{\rm n}=180\,000~{\rm g~mol}^{-1}$)-*b*-P2VP($M_{\rm n}=77\,000~{\rm g~mol}^{-1}$) (PDI = 1.09) (Polymer Source. Inc.) solution in chloroform was prepared and spin-coated on silicon wafers at 2000 rpm for 30 s. The resulting film was characterized with tapping mode AFM (Bruker Dimension Icon). The silicon wafer was then placed on a stand in a glass jar with the stand surrounded by a pool of chloroform. The jar was firmly sealed with its lid and the film was left to solvent anneal for the desired time. Subsequently, the lid of the jar was removed and the wafer piece removed. Films were solvent annealed for 7:30, 10:00, 11:15, 12:30, 13:45, 14:23, 15:00, 16:15, 17:30 where the first number in the format x:y is minutes and the second number is seconds. The solvent annealed films were characterized with AFM in tapping mode.

Films solvent annealed for 14:23 were imaged with SEM. For SEM imaging solvent annealed films were stained with iodine. A film was stained with iodine by placing it in a jar with iodine, sealing the jar, and placing the jar in an oven at 50 °C for 3 hours. The films were imaged top-down with SEM (JEOL JSM-7500F Field Emission Scanning Electron Microscope) using the Low Angle Backscatter (LABe) detector. The wafers supporting the iodine stained films were also cleaved in two and the film cross-sections were imaged with SEM using the LABe detector.

Preparation and characterization of PS-b-P2VP-AuNR101 and PS-b-P2VP-AuNR70 nanocomposite films

PS-*b*-P2VP-AuNR101 and PS-*b*-P2VP-AuNR70 nanocomposite films were prepared and characterized the same way except PS-*b*-P2VP-AuNR101 nanocomposite films were prepared with the synthesized 101 nm length by 16 nm diameter AuNRs while PS-*b*-P2VP-AuNR70 nanocomposite films were prepared with 70 nm length by 12 nm diameter AuNRs purchased from nanoComposix, Inc. (surface: sodium citrate).

Soft Matter Paper

Nanocomposite films were prepared as follows. A solution of AuNRs in water was centrifuged at 9289g for 30 minutes (Eppendorf Centrifuge 5804). The supernatant was removed and the concentrated AuNRs at the bottom of the centrifuge tube were added to a 10 ml solution of P2VP-SH ($M_n = 2500 \text{ g mol}^{-1}$, PDI = 1.16) (Polymer Source. Inc.) in N,N-dimethylformamide (DMF) while the solution was stirring. The solution was then stirred overnight. The solution was subsequently centrifuged at 9289g for 30 minutes and the supernatant removed. 10 ml of DMF was then added to the centrifuge tube and the AuNRs were resuspended. The solution was then transferred to a new centrifuge tube and centrifuged at 9289g for 30 minutes. The supernatant was removed and 10 ml of DMF was added. The AuNRs were resuspended and the solution was transferred to a new centrifuge tube. The solution was then centrifuged at 9289g for 30 minutes and the supernatant was removed. The concentrated AuNRs at the bottom of the centrifuge tube were then added to a stirring 1 ml 2 wt% $PS(M_n = 180\,000 \text{ g mol}^{-1})-b-P2VP(M_n = 180\,000 \text{ g mol}^{-1})$ $77\,000 \text{ g mol}^{-1}$) (PDI = 1.09) in chloroform solution and the solution was stirred for 2 hours. The solution was subsequently spin-coated on silicon wafers at 2000 rpm for 30 s. The films were solvent annealed in chloroform for 14 minutes 23 seconds in an identical fashion to the neat films. The surfaces of the solvent annealed films were characterized with AFM in tapping mode. The solvent annealed films were also characterized with SEM topdown using the LABe detector. The films' cross-sections were imaged with SEM using the LABe detector by cleaving the wafers supporting the films in half.

Definition of an AuNR away from defects in the vertical cylinder lattice

For an AuNR in the bridging state we define the AuNR as away from defects in the vertical cylinder lattice as follows. Given a perfect hexagonal lattice of vertical cylinders with an AuNR in the bridging state we take the two vertical cylinders being bridged by the AuNR and which are colored red in Fig. S5 (ESI†). We then take the nearest neighbor cylinders of the two red cylinders, which are colored green in Fig. S5 (ESI†). Finally, we take the nearest neighbor cylinders of the green cylinders, which are colored blue in Fig. S5 (ESI†). For an experimentally observed AuNR in the bridging state if the vertical cylinder lattice around the AuNR does not deviate substantially from the perfect hexagonal lattice in the region of the lattice corresponding to the green and blue cylinders, the AuNR is away from defects in the lattice.

For an AuNR in the centered state we defined it as away from defects in the vertical cylinder lattice as follows. Given a perfect hexagonal lattice of vertical cylinders with an AuNR in the centered state we take the vertical cylinder into the top of which the AuNR is embedded, colored red in Fig. S6 (ESI†). We then take the nearest neighbor cylinders of the red cylinder, which are colored green in Fig. S6 (ESI†). Then we take the nearest neighbor cylinders of the green cylinders, which are colored blue in Fig. S6 (ESI†). For an experimentally observed AuNR in the centered state if the vertical cylinder lattice around the AuNR does not deviate substantially from the perfect

hexagonal lattice in the region of the lattice corresponding to the green and blue cylinders, the AuNR is away from defects in the lattice.

Hybrid particle-field theory simulations

HPFT is a framework developed by Sides $et~al.^{31}$ in which particles are treated as fixed cavity functions and mean-field polymer distributions are calculated around them. Our mean-field HPFT simulations consisted of an A–B diblock copolymer and an explicit nanorod confined between two neutral surfaces in a weakly compressible system. The diblock chain was modeled as a discrete Gaussian chain of length N=60 segments and was biased by an initial field configuration to form vertical cylinders. The nanorod was modeled as a fixed, bare, A-like particle. The enthalpic repulsion between A and B segments was set to $\chi N=30$. Polymer free energy differences between different states (particle diameter, length, and orientation) was calculated from differences in the effective Hamiltonian. More complete details of the model parameters and equations are given in the ESI.†

Conflicts of interest

There are no conflicts to declare.

Acknowledgements

This research was supported primarily by the National Science Foundation (NSF) POLYMERS-DMR-1905912, with secondary support from MRSEC-DMR-1720530 (B. R., R. J. C., X. Y., C. B. M.), NSF CBET-1510635 (R. A. R.) and PIRE-OISE-1545884 (R. J. C., C. B. M., R. A. R.). Initial support was provided by E. I. du Pont de Nemours & Co. Computational resources were made available at the National Institute for Computational Sciences, Texas Advanced Computing Center, and San Diego Supercomputer Center through XSEDE award TG-DMR150034. We acknowledge the Nanoscale Characterization Facility and the Scanning and Local Probe Facility at the Singh Center for Nanotechnology. We would like to thank Nadia M. Krook, Hyun-Su Lee, and Eric J. Bailey for insightful scientific discussions.

References

- 1 S. A. Maier, P. G. Kik, H. A. Atwater, S. Meltzer, E. Harel, B. E. Koel and A. A. G. Requicha, Local detection of electromagnetic energy transport below the diffraction limit in metal nanoparticle plasmon waveguides, *Nat. Mater.*, 2003, 2(4), 229–232.
- 2 V. Abetz and P. F. W. Simon, Phase Behaviour and Morphologies of Block Copolymers, in *Block Copolymers I*, ed. V. Abetz, Springer Berlin Heidelberg, Berlin, Heidelberg, 2005, pp 125–212.
- 3 M. R. Bockstaller, R. A. Mickiewicz and E. L. Thomas, Block copolymer nanocomposites: Perspectives for tailored functional materials, *Adv. Mater.*, 2005, **17**(11), 1331–1349.

- 4 J. Kao, K. Thorkelsson, P. Bai, B. J. Rancatore and T. Xu, Toward functional nanocomposites: taking the best of nanoparticles, polymers, and small molecules, *Chem. Soc. Rev.*, 2013, 42(7), 2654–2678.
- 5 J. J. Chiu, B. J. Kim, E. J. Kramer and D. J. Pine, Control of nanoparticle location in block copolymers, *J. Am. Chem. Soc.*, 2005, 127(14), 5036–5037.
- 6 B. J. Kim, J. Bang, C. J. Hawker and E. J. Kramer, Effect of areal chain density on the location of polymer-modified gold nanoparticles in a block copolymer template, *Macro-molecules*, 2006, 39(12), 4108–4114.
- 7 B. J. Kim, G. H. Fredrickson and E. J. Kramer, Effect of polymer ligand molecular weight on polymer-coated nanoparticle location in block copolymers, *Macromolecules*, 2008, 41(2), 436–447.
- 8 M. R. Bockstaller, Y. Lapetnikov, S. Margel and E. L. Thomas, Size-selective organization of enthalpic compatibilized nanocrystals in ternary block copolymer/particle mixtures, *J. Am. Chem. Soc.*, 2003, **125**(18), 5276–5277.
- 9 Y. Lin, A. Boker, J. B. He, K. Sill, H. Q. Xiang, C. Abetz, X. F. Li, J. Wang, T. Emrick, S. Long, Q. Wang, A. Balazs and T. P. Russell, Self-directed self-assembly of nanoparticle/copolymer mixtures, *Nature*, 2005, 434(7029), 55–59.
- 10 H. Kang, F. A. Detcheverry, A. N. Mangham, M. P. Stoykovich, K. C. Daoulas, R. J. Hamers, M. Muller, J. J. de Pablo and P. F. Nealey, Hierarchical assembly of nanoparticle superstructures from block copolymernanoparticle composites, *Phys. Rev. Lett.*, 2008, 100, 14.
- 11 Y. Zhao, K. Thorkelsson, A. J. Mastroianni, T. Schilling, J. M. Luther, B. J. Rancatore, K. Matsunaga, H. Jinnai, Y. Wu, D. Poulsen, J. M. J. Frechet, A. P. Alivisatos and T. Xu, Small-molecule-directed nanoparticle assembly towards stimuli-responsive nanocomposites, *Nat. Mater.*, 2009, 8(12), 979–985.
- 12 R. D. Deshmukh, Y. Liu and R. J. Composto, Two-dimensional confinement of nanorods in block copolymer domains, *Nano Lett.*, 2007, 7(12), 3662–3668.
- 13 K. Thorkelsson, A. J. Mastroianni, P. Ercius and T. Xu, Direct Nanorod Assembly Using Block Copolymer-Based Supramolecules, *Nano Lett.*, 2012, **12**(1), 498–504.
- 14 K. Thorkelsson, J. H. Nelson, A. P. Alivisatos and T. Xu, Endto-End Alignment of Nanorods in Thin Films, *Nano Lett.*, 2013, 13(10), 4908–4913.
- 15 K. Thorkelsson, N. Bronstein and T. Xu, Nanorod-Based Supramolecular Nanocomposites: Effects of Nanorod Length, *Macromolecules*, 2016, **49**(17), 6669–6677.
- 16 A. Halevi, S. Halivni, M. Oded, A. H. E. Muller, U. Banin and R. Shenhar, Co-Assembly of A-B Diblock Copolymers with B'-type Nanoparticles in Thin Films: Effect of Copolymer Composition and Nanoparticle Shape, *Macromolecules*, 2014, 47(9), 3022–3032.
- 17 E. Ploshnik, A. Salant, U. Banin and R. Shenhar, Hierarchical Surface Patterns of Nanorods Obtained by Co-Assembly with Block Copolymers in Ultrathin Films, *Adv. Mater.*, 2010, **22**(25), 2774–2779.

18 E. Ploshnik, A. Salant, U. Banin and R. Shenhar, Coassembly of block copolymers and nanorods in ultrathin films: effects of copolymer size and nanorod filling fraction, *Phys. Chem. Chem. Phys.*, 2010, 12(38), 11885–11893.

- 19 B. Rasin, H. K. Chao, G. Q. Jiang, D. L. Wang, R. A. Riggleman and R. J. Composto, Dispersion and alignment of nanorods in cylindrical block copolymer thin films, *Soft Matter*, 2016, **12**(7), 2177–2185.
- 20 C. A. Breen, T. Deng, T. Breiner, E. L. Thomas and T. M. Swager, Polarized photoluminescence from poly(p-phenylene-ethynylene) via a block copolymer nanotemplate, *J. Am. Chem. Soc.*, 2003, **125**(33), 9942–9943.
- 21 N. M. Krook, J. Ford, M. Marechal, P. Rannou, J. S. Meth, C. B. Murray and R. J. Composto, Alignment of Nanoplates in Lamellar Diblock Copolymer Domains and the Effect of Particle Volume Fraction on Phase Behavior, ACS Macro Lett., 2018, 7(12), 1400–1407.
- 22 S. W. Hsu and T. Xu, Tailoring Co-assembly of Nanodiscs and Block Copolymer-Based Supramolecules by Manipulating Interparticle Interactions, *Macromolecules*, 2019, 52(7), 2833–2842.
- 23 J. Yin, X. P. Yao, J. Y. Liou, W. Sun, Y. S. Sun and Y. Wang, Membranes with Highly Ordered Straight Nanopores by Selective Swelling of Fast Perpendicularly Aligned Block Copolymers, ACS Nano, 2013, 7(11), 9961–9974.
- 24 X. D. Gu, I. Gunkel, A. Hexemer, W. Y. Gu and T. P. Russell, An *In Situ* Grazing Incidence X-Ray Scatterings Study of Block Copolymer Thin Films During Solvent Vapor Annealing, *Adv. Mater.*, 2014, **26**(2), 273–281.
- 25 X. D. Gu, I. Gunkel, A. Hexemer and T. P. Russell, Controlling Domain Spacing and Grain Size in Cylindrical Block Copolymer Thin Films by Means of Thermal and Solvent Vapor Annealing, *Macromolecules*, 2016, 49(9), 3373–3381.
- 26 A. V. Berezkin, C. M. Papadakis and I. I. Potemkin, Vertical Domain Orientation in Cylinder-Forming Diblock Copolymer Films upon Solvent Vapor Annealing, *Macromolecules*, 2016, 49(1), 415–424.
- 27 H. Elbs and G. Krausch, Ellipsometric determination of Flory-Huggins interaction parameters in solution, *Polymer*, 2004, 45(23), 7935–7942.
- 28 K. Tanaka, A. Takahara and T. Kajiyama, Film thickness dependence of the surface structure of immiscible polystyrene/poly(methyl methacrylate) blends, *Macromolecules*, 1996, **29**(9), 3232–3239.
- 29 H. K. Chao, J. Koski and R. A. Riggleman, Solvent vapor annealing in block copolymer nanocomposite films: a dynamic mean field approach, *Soft Matter*, 2017, **13**(1), 239–249.
- 30 X. C. Ye, C. Zheng, J. Chen, Y. Z. Gao and C. B. Murray, Using Binary Surfactant Mixtures To Simultaneously Improve the Dimensional Tunability and Monodispersity in the Seeded Growth of Gold Nanorods, *Nano Lett.*, 2013, 13(2), 765–771.
- 31 S. W. Sides, B. J. Kim, E. J. Kramer and G. H. Fredrickson, Hybrid Particle-Field Simulations of Polymer Nanocomposites, *Phys. Rev. Lett.*, 2006, **96**(25), 250601.